International Journal of Pharmaceutics 417 (2011) 151–162

Contents lists available at ScienceDirect

International Journal of Pharmaceutics

journal homepage: www.elsevier.com/locate/ijpharm

Raman mapping of pharmaceuticals

Keith C. Gordon[a], Cushla M. McGoverin[b,*]

[a] MacDiarmid Institute for Advanced Materials and Nanotechnology, Chemistry Department, University of Otago, Dunedin 9054, New Zealand
[b] Department of Food Science, Stellenbosch University, Private Bag XI, Stellenbosch 7602, South Africa

ARTICLE INFO

Article history:
Received 30 September 2010
Received in revised form
21 December 2010
Accepted 21 December 2010
Available online 29 December 2010

Keywords:
Raman spectroscopy
Mapping
Imaging
Confocal
Chemometrics

ABSTRACT

Raman spectroscopy may be implemented through a microscope to provide fine scale axial and lateral chemical maps. The molecular structure of many drugs makes Raman spectroscopy particularly well suited to the investigation of pharmaceutical systems. Chemometric methods currently used to assess bulk Raman spectroscopic data are typically applied to Raman mapping data from pharmaceuticals; few reports exist where the spatial information inherent to a mapped dataset is used for the calculation of chemical maps. Both univariate and multivariate methods have been applied to Raman mapping data to determine the distribution of active pharmaceutical ingredients (APIs) in tablets, solid dispersions for increased solubility and controlled release devices. The ability to axially (depth) profile using Raman mapping has been used in studies of API penetration through membranes, cellular uptake of drug delivery liposomes, and initial API distribution and subsequent elution from coatings of medical devices. New instrumental developments will increase the efficiency of Raman mapping and lead to greater utilisation of Raman mapping for analyses of pharmaceutical systems.

1. Introduction

1.1. Raman spectroscopy

The Raman effect was first reported by Sir C.V. Raman in 1928 (Raman, 1928; Raman and Krishnan, 1928, 1929) and is the inelastic scattering of light. Incident photons lose or gain energy by interaction with the sample, the loss of incident photon energy is a much stronger effect and is termed Stokes scattering – the reverse process, in which the incident photons gain energy, is known as anti-Stokes scattering (Fig. 1). In the context of pharmaceutical samples almost all spectra are due to Stokes scattering, with sample-photon interactions primarily involving vibrational modes of the sample molecules (Smith and Dent, 2005). Raman scattering therefore reflects the vibrational energies of the molecules within samples; these in turn are related to the nature of the bonding within the compounds of interest (Long, 2005). Thus Raman spectroscopy probes the same range of energies as infrared spectroscopy, however, the selection rules for Raman transitions differ from the infrared. In the case of infrared transitions, the dipole moment associated with a molecular vibration determines the intensity of the transition. This is not the case for Raman scattering which relies upon: (1) the creation of an induced dipole (polarization) in the molecule; (2) the modification of this dipole by molecular vibration; (3) the subsequent scattering of a photon from this modified oscillating dipole (Long, 2002). Raman spectra are presented as the difference in energy (in wavenumbers) between incident and scattered light, therefore in a Raman spectrum the wavenumber will be the same for a specific mode in a specific molecule, regardless of the excitation wavelength (a stretch at 1600 cm^{-1} will occur whether the source is 1064 or 514 nm). As Raman transitions are due to inelastic scattering phenomena they are inherently rare events, hence Raman spectra are weak and low concentrations of analyte may be difficult to observe. Raman transitions are also much weaker than the elastic scattering of the excitation source – the Raleigh scattering. Optics that block Raleigh scattering, single stage spectrographs, and sensitive charge-coupled device (CCD) detectors have transitioned Raman spectroscopy beyond academic applications and into the industrial realm (McCreery, 2000).

The differing physical phenomena that underpin Raman and infrared spectroscopy mean that strong infrared bands need not be intense in Raman spectra and vice versa. The most striking example of this is for water, the infrared spectrum of water is intense causing a great deal of difficulty in using infrared in aqueous systems – however the Raman spectrum of water is weak and there is generally no difficulty in collecting Raman data from aqueous samples. The reasons for this are directly related to the electronic structure of water – it is a σ-bonded structure which has a strong dipole moment, hence the vibrations are infrared active, but the electrons are not easily polarized and thus dipole induction is difficult and Raman scattering is weak. In general molecules that possess π-electrons, such as many active pharmaceutical ingredi-

* Corresponding author. Tel.: +27 21 808 3578; fax: +27 21 808 3510.
E-mail address: cushla@sun.ac.za (C.M. McGoverin).

0378-5173/$ – see front matter © 2011 Elsevier B.V. All rights reserved.
doi:10.1016/j.ijpharm.2010.12.030

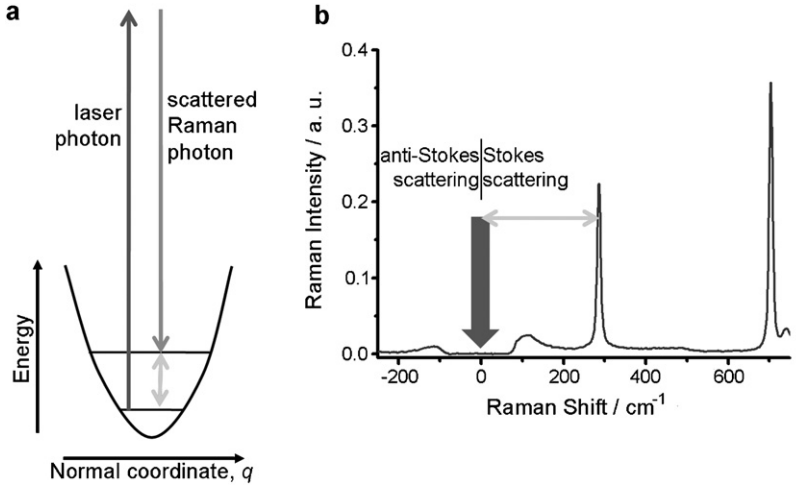

Fig. 1. (a) Raman scattering, the basis of Raman spectroscopy, is a coherent two photon event. Photons that have been Raman scattered have either lost or gained energy equivalent to that of a molecular vibration. Stokes scattering involves an energy loss and is the most common form of Raman scattering. (b) Raman spectra are depicted in terms of the energy difference between the incident and scattered photons, by convention Stokes scattering is positive. Each peak (band) in a Raman spectrum corresponds to a molecular vibration inherent to the analysed sample.

ents (APIs), show strong Raman scattering because they are easily polarized, conversely compounds which are primarily σ-bonded, such as excipients, may be very weak Raman scatterers.

1.2. Raman microscopy

Raman spectroscopic experiments may be carried out using microscope optics to guide the excitation laser and collect the resulting Raman scattering. The use of visible wavelength lasers means that when using a microscope spatial resolution and spot sizes down to a 1 μm diameter may be achieved. When using confocal microscopy a small well-defined volume of the sample is analysed. The dimensions of this volume are determined by the spot size (lateral resolution) of the irradiating laser and the depth of field (depth resolution) of the microscope. The lateral resolution of Raman microscopes is largely determined by the excitation wavelength and the numerical aperture of the objective. If one assumes the objective lens is filled by a beam of uniform intensity, the Airy disc approximation, then the focused spot diameter, d is given by Eq. (1):

$$d = \frac{1.22\lambda}{\mathrm{NA}} \quad (1)$$

in which λ is the laser wavelength and NA is the numerical aperture of the objective. For example 785 nm excitation and a 100× objective with NA = 0.9 gives a spot size of 1.06 μm. This deals with lateral resolution, at least to a first approximation, but the depth of the image from which Raman scattering is collected is not well controlled until a confocal configuration is applied to the experiment. A confocal microscope limits the depth of field by placing a pinhole aperture in the path between the objective and detector (Fig. 2). The confocal advantage may be applied to Raman microscopes such that a minor improvement to lateral resolution, and a major improvement to axial resolution, is made.

An element of caution is required when analysing confocal Raman data. Instrument manufacturers report axial resolution of Raman confocal microscopes as the full width at half maximum (FWHM) of the 520 cm^{-1} band of silicon as the focus is scanned through the air/silicon wafer interface. This a well defined test and certainly provides the axial resolution for *such an experiment*; however, when examining a buried structure or sample beneath a glass coverslip this axial resolution test underestimates the sampled depth of field.

In a series of studies Everall et al. (Everall, 2000a,b; Everall et al., 2007) have investigated the difference between the theoretical operation of a confocal microscope and the reality of performance with realistic rather than idealized samples. In principal the depth resolution (DR) is given by Eq. (2) (Juang, 1998):

$$\mathrm{DR} = \frac{2.2n\lambda}{\pi(\mathrm{NA})^2} \quad (2)$$

in which n is the refractive index of the material, λ is the laser wavelength and NA is the numerical aperture of the objective. This equation suggests that the DR may be improved simply by increasing NA. Indeed for a typical excitation source, such as 532 nm, and an objective with NA = 0.95 and material of n = 1.5 the DR = 600 nm. Everall examined a variety of substrates in which materials of differing refractive index were layered and found that the depth resolution was a complicated function related to the refractive

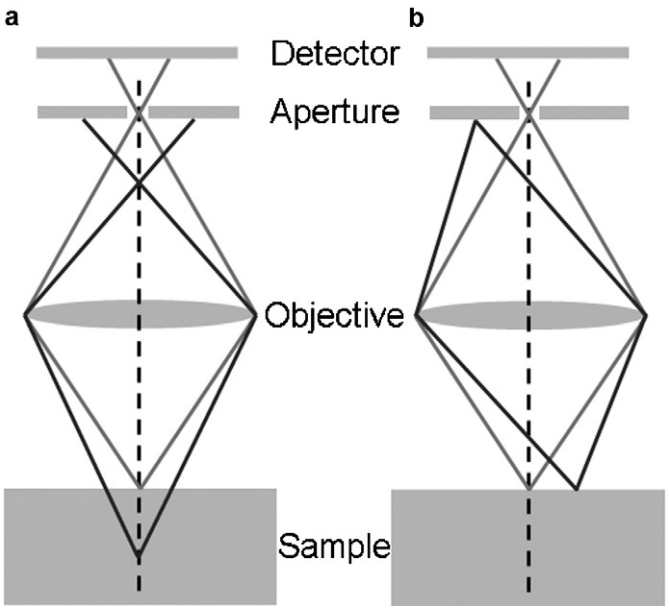

Fig. 2. A confocal aperture allows depth of field to be controlled and enables axial profiling. Only Raman scattering from the focal point (thin gray line) is focused through the confocal aperture. Scattering outside the focal point (thin black line), either axially (a) or laterally (b), is blocked.

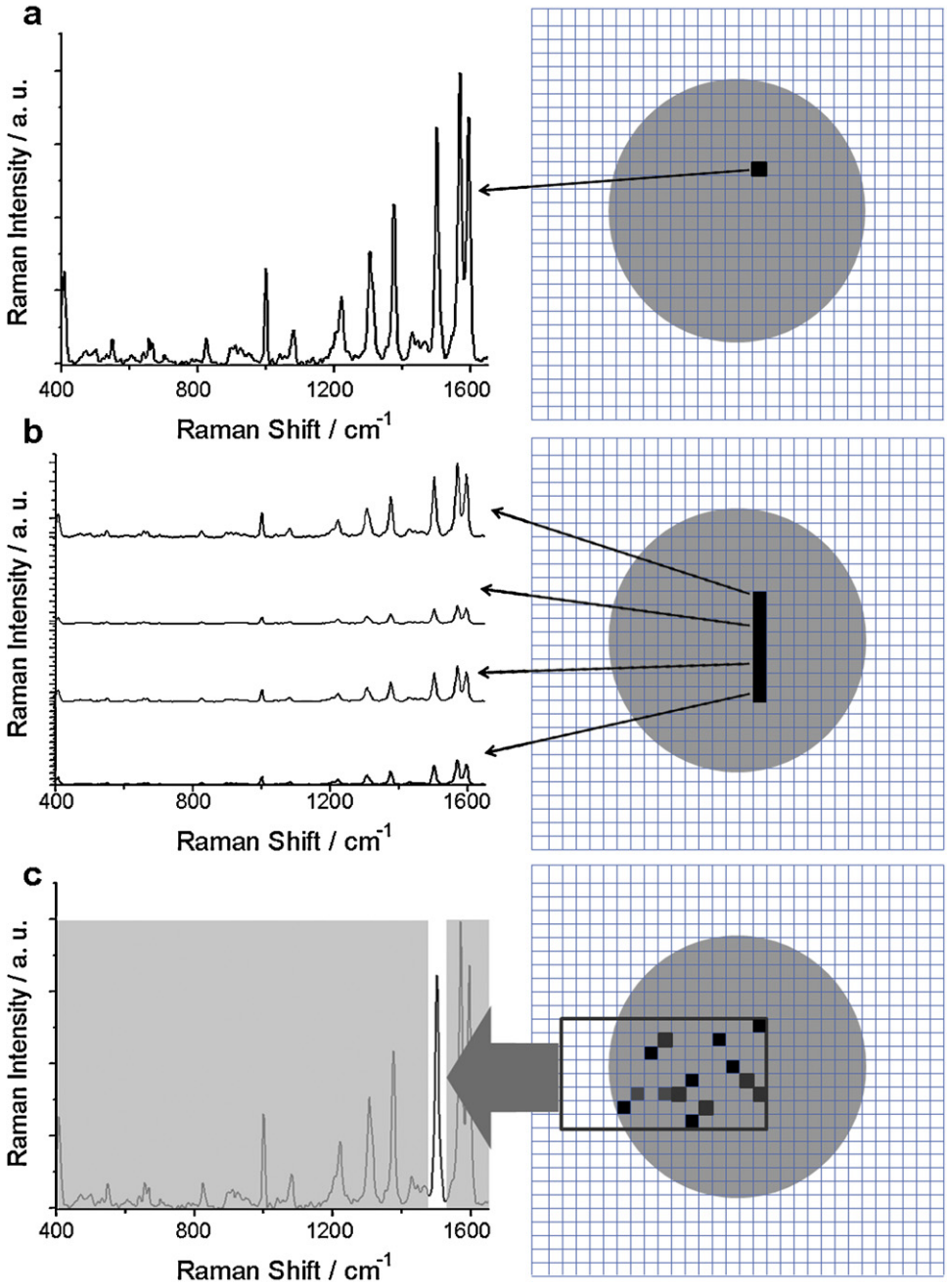

Fig. 3. Schematic representations of mapping pixels on a sample. (a) A point scan system measures each spectrum individually at a series of predefined points, one is shown. (b) In a line scan system several spectra are collected simultaneously from adjacent points within the region of interest. (c) In a global configuration a comparatively large area is illuminated and the intensity of a single peak range simultaneously recorded for all points within the area.

index of the component materials in the sample and the optical nature of the experiment; furthermore the depth resolution was variable depending on the sampling depth in the structure of interest. When comparing FWHM of a bare silicon wafer and one buried beneath a glass coverslip (recorded using a dry metallurgical 100× objective (0.9 NA)) a fivefold increase was observed (DR increased from 2.1 μm to 10.0 μm). A depth scale compression was also observed when examining the silicon wafer beneath a coverslip. The silicon response had a maximum near 100 μm, rather than at the 158 μm predicted (Everall et al., 2007). The reality is that most pharmaceutical samples comprise of layers and heterogeneous solid state mixtures, this means that depth resolution for these sorts of samples is a function of the sample as much as it is of the instrument. The ideal resolution of 600 nm is unachievable and it has been shown that the DR is often five times greater than the Eq. (2) limit (Tabaksblat et al., 1992). Two methods are commonly put forward to reduce this axial resolution problem; firstly scan across an axial cross-section or second use an immersion objective to reduce refractive indices changes from objective to sample.

Lateral resolution may be improved beyond the diffraction limit (Eq. (1)) by using near field optics. These are systems in which the excitation source is compressed through an optical fibre. This results in spatial resolution superior to that available through diffractive optics. A number of instruments now possess such near-field configurations and thus can acquire data down to 100 nm resolution (Deckert et al., 1998). However near-field images are limited to the surface of the substrate and thus cannot depth profile.

1.3. Raman mapping

Raman mapping involves the collection of spectral data from discrete sections of an area or volume (Fig. 3). There are two methods to implement Raman mapping. The first requires translational motion of the sample between each discrete measurement. A point source is used to irradiate an area and the collected Raman scattering is imaged into a spectrograph and diffracted across the face of a CCD detector (Fig. 3a). A CCD is comprised of pixels able to detect light and which can be individually addressed; typically the pixels are of the order of 25 μm × 25 μm in area and the overall detector is up to 5 cm long and 1 cm high. The spectral width observed is dependent on the spectrograph dispersion characteristics and the length of the detector. The process can be made faster by using an irradiating line rather than a point and translating the sample underneath the line image (Fig. 3b). This method works because the CCD detector has a height corresponding to the line. The result of these types of experiments is a mapped area or cube, if depth resolution is altered, in which each point contains spectral information.

An alternate way to map a sample is to utilize the area nature of the CCD. Effectively the CCD has a large area imaged on to it and each individual pixel within the CCD is measured. From this the spectral properties at each area element may be ascertained. However the Raman scattering coming from the sample cannot be simultaneously measured over all wavenumbers – rather a filter is placed between the incoming Raman scattering and the CCD. Thus at any one moment the CCD is observing only a discrete wavenumber slice of the overall Raman section (Fig. 3c). Acousto-optic tuneable filters (AOTFs) and liquid crystal tuneable filters (LCTFs) can be used to scan through the entire spectrum (Pappas et al., 2000). This method is called the global image method and has the advantage of involving no movement of the sample. Often the two methods of obtaining spatially resolved Raman spectral data are differentiated using the terms mapping and imaging: mapping when sample motion is involved and imaging when there is no sample movement.

1.4. Data analysis

Spatially resolved Raman data were originally analysed with only univariate techniques, but increasing sample complexity has driven data analysis towards multivariate approaches. Univariate analyses require a constituent-specific spectral band that is free of interference from other constituents in the system. Such bands are characterised either by position, area, height or full width at half maximum height (FWHM), and the chosen characteristic is plotted as a function of spatial coordinates (i.e., mapped). The interference-free constituent-specific band requirement for univariate analyses necessitates spectral characterisation of the system components prior to Raman mapping. Information regarding the spectra of each constituent is required to determine if and where an interference-free constituent-specific band occurs. In more complex systems where interference-free constituent-specific spectral bands are not present, multivariate methods (which use regions of spectral data) are instead applied (Geladi and Grahn, 1997; Grahn and Geladi, 2007). Multivariate methods used to the analyse Raman mapping data collected from pharmaceutical systems include *K*-means clustering (KM) (Zhang et al., 2005), direct classical least squares (DCLS) (Vajna et al., 2010; Zhang et al., 2005), augmented classical least squares (ACLS) (Belu et al., 2008), principal components analysis (PCA) (Bell et al., 2007; Zhang et al., 2005) and multivariate curve resolution (MCR) (Zhang et al., 2005). Each multivariate method yields a score or parameter for each Raman spectrum. Subsequently, these scores or parameters are mapped as a function of spatial coordinates. Several multivariate methods (e.g., PCA, MCR) do not require *a priori* spectral information, unlike univariate methods. In practice, however, constituent-specific spectral information is desirable for interpretation of results.

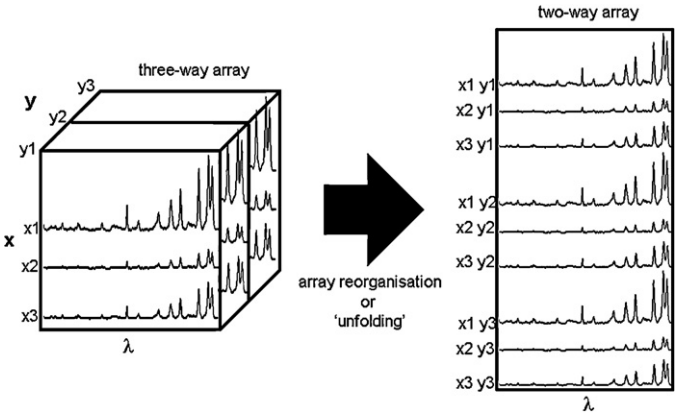

Fig. 4. Illustration of the reorganization of the three way array collected in a mapping experiment into a two way array for analysis using multivariate methods. Adapted from Andrew and Hancewicz (1998).

Multivariate methods generally use a two-way data matrix and require three-way arrays (*x*, *y* spatial coordinates and wavelength (λ)) to be 'unfolded' before analysis (Fig. 4) (Andrew and Hancewicz, 1998). Unfolding is normally done by placing spectral data from one line of the image after another line of the image to form a two-way matrix. In essence, the spatial information is set aside during spectral analysis and is only used in the plotting of the scores/parameters generated by the analysis.

Univariate and multivariate methods were compared using a computational model pharmaceutical system (Šašić et al., 2004) and a related tablet system manufactured using two different techniques (Šašić, 2007a). Each method was used to determine the distribution of API and excipients in the tablets. In both cases the quality of compositional images was improved by the use of multivariate techniques, though even in case of partially overlapped bands univariate analyses gave reasonably concurrent results for major components (Šašić, 2007a). The application of PCA in the Šašić (2007a) study cautioned against using the amount of spectral variance explained by a principal component (PC) to determine whether the respective scores values should be examined. In the systems studied the explained variance parameter suggested just the first two or three PCs should be examined, however, the eighth to twelfth PC loadings contained features concurrent with the peaks of magnesium stearate, a constituent present at ~1%.

In addition to comparing univariate and multivariate methods this study also examined the importance of thresholding in the production of a composite image. A composite image is a single image illustrating the distribution of all components and is often the goal of a Raman mapping experiment. To generate a composite image component-specific thresholds must be set to determine which regions are unique to that constituent. In the study of Šašić (2007a) the commercially available Otsu's algorithm, which maximises between-class variance, was used to set threshold levels for binarization of each component. The resulting binarized pixels of the four components (magnesium stearate was not included) were too numerous for the total number of available pixels in the composite image. Simple addition of the binarized images for each of the components would result in a composite image with severe overlap despite the fact that the thresholds set by Otsu's algorithm did not indicate there was a problem. The consequence of this was that new thresholds were set in a subjective manner and consequently the composite image was to an extent arbitrary. This thresholding problem will be exacerbated by more intimately mixed samples and increased sampling depth. While it is often desirable for illus-

tration purposes to have a composite image it is perhaps more expedient for interpretation to map components separately; at the very least presentation of a composite image should be accompanied by a thorough description of thresholds applied.

Quantitative compositional maps would further simplify the problems associated with the production of composite images. Within current literature the presentation of constituent distribution, as determined by Raman mapping, has largely been completed in a qualitative sense. Quantitative compositional maps generally require calibration of the Raman signal to assign a concentration to each pixel of the image. As with qualitative visualisation this may be completed in a univariate or multivariate way, though multivariate methods are likely to be more accurate. The Raman signal is proportional to concentration when all other experimental parameters are constant. The production of quantitative images often requires the calibration of Raman signal alterations with changing constituent concentration, whether this is the peak area of a univariate analysis or the shape of spectra in a multivariate analysis. Image construction requires the mapping of samples with known concentrations, averaging all the spectra within the mapped area and calibration using these known concentrations and this averaged spectrum. Once a reliable calibration has been calculated it may be applied to each pixel within the mapped area to determine concentration of the specified constituent. This procedure is dependent on the area from which spectra are averaged being representative of the sample concentration. It is for this reason perhaps that quantitative imaging is more prevalent within the field of near infrared (NIR) mapping (Gendrin et al., 2008; Hamad et al., 2007; Kolomiets et al., 2008) where large sample areas may be imaged in a fraction of the time typically required for Raman chemical imaging.

The need for prior calibration has inhibited the widespread calculation of quantitative compositional maps. Several methods of analysis that eliminate the need for calibration have been examined, for example, multivariate curve resolution-alternating least squares (MCR-ALS) (Amigo and Ravn, 2009) and classical least squares (CLS) (Amigo and Ravn, 2009; Gendrin et al., 2007). Classical least squares requires the pure spectra of all components, an often satisfiable condition in pharmaceutical applications such as tablet manufacture (Amigo et al., 2008; Cruz et al., 2009). Each pixel's spectrum is treated as the sum of all constituents scaled by their concentration. The consequence of this is that interactions between analytes and non-systematic variations within the spectra are not modelled and interfere with concentration estimates. Multivariate curve resolution-alternating least squares is not constrained by pure spectra and iteratively predicts pure spectra and concentrations (Amigo et al., 2008; Amigo and Ravn, 2009). Multivariate curve resolution-alternating least squares requires initial spectral estimates, the quality of which influences the quality of concentration estimates, and constraints must be applied, e.g., non-negativity of spectra and concentrations (Duponchel et al., 2003). This type of analysis suffers when applied to homogenous samples; the presence of pixels/areas attributable to each component is required for successful analyses. Augmented MCR-ALS minimises this problem – the homogenous data set is augmented with data sets recorded from the pure components (Cruz et al., 2009). The most appropriate data analysis method is dependent on the complexity of the investigated system and the type of information that is to be generated and therefore several methods of analyses will be tested.

Several chemometric techniques used to analyse constituent distribution within a model tablet formulation were compared (Zhang et al., 2005). A model bilayer tablet was made; one side contained 76% (w/w) lactose, 20% (w/w) avicel, 2% (w/w) magnesium stearate and 2% (w/w) red dye (FD&C red #40), and the other side contained 74% (w/w) lactose, 19% (w/w) avicel, 2% (w/w) magnesium stearate and 5% (w/w) sodium benzoate. Sodium benzoate was the only compound containing aromatic functionality and served as an API substitute; only the side containing sodium benzoate was Raman mapped. A 785 nm excitation wavelength through a 50× objective (NA 0.55) was used to map a 400 μm × 400 μm area in 10 μm lateral increments. Each spectrum was recorded from 715.7 to 1265.6 cm^{-1}, with a spectral sampling interval of 0.96 cm^{-1}. Laser induced heating caused sample scorching along the last line of sampling and these data were discarded. Visual inspection of the spectral data indicated both ends of the spectra were noisy, however, and only data from 745.3 to 1208.1 cm^{-1} were included in subsequent analyses. The result was a three-dimensional imaging data cube with the dimensions of $40 \times 41 \times 484$.

Two different preprocessing methods were applied independently: (1) standard normal variate (SNV) transformation was used prior to PCA and cluster analysis, and (2) Savitzky–Golay second derivative transformation was used prior to DCLS and MCR. Standard normal variate preprocessing was only applied prior to qualitative analyses as the scaling involved in this transformation may have resulted in a loss of quantitative information. The scaling of SNV is determined by the spectral contribution of all constituents within the spectrum, and hence scaling is influenced by constituent concentration. Scaling in SNV can therefore alter the representation of constituents between spectra, which would have consequences for subsequent statistical analyses.

Principal components analysis was performed on SNV transformed data, and each constituent was identified in the PCs calculated from this data cube. Principal component one featured mostly lactose peaks with some avicel bands, PC2 aligned with sodium benzoate, and PC3 could be attributed to avicel. Peaks coincident with those of magnesium stearate were observed in PC7. Spectral assignments were based on visual inspection and the calculation of correlation coefficients between PC loadings and the pure component spectra. Scores of the first seven PCs were used in both KM and Fuzzy C-means (FCM) cluster analyses. Three clusters were considered appropriate when using either clustering method. The centre of each cluster was compared to pure component spectra by correlation analysis and visual inspection; the three clusters were identified as lactose, avicel and sodium benzoate.

Application of DCLS analysis also indicated the spectral contribution of magnesium stearate was weak within the data cube. Use of a four component model in the DCLS analyses lead to overfitting; a better fit was achieved using a three component lactose, avicel and sodium benzoate model. Magnesium stearate was not observed when either MCR simple-to-use interactive self-modeling mixture analysis (SIMPLISMA) or ALS methods were used. The distribution of each component/PC was visualised in 64-element grayscale maps. The influence of outlying pixels within these maps was minimised by setting d_{min} and d_{max} values that defined the range as the central 95% of pixels within the image. The 2.5% of pixels that had values lower or higher than d_{min} and d_{max} were set to d_{min} and d_{max} respectively, and a linear scale was used between d_{min} and d_{max}. Red, green, blue images were used to visualise the distribution of all three components (sodium benzoate, lactose and avicel, respectively) in the same image. The resulting component distributions from each method were similar. The PCA scores and DCLS concentration images differed most significantly with respect to acivel distribution, which may have been a consequence of the 'mixture' effect of PC loadings. The clustering and DCLS images differed in terms of boundaries, e.g., sodium benzoate inhabited larger areas in the clustering images than the DCLS image. This may have been a consequence of the equal population tendency of clustering algorithms. In the KM clustering image there is a loss of contrast as a pixel must be assigned to just one class; in FCM clustering, intensity variation within a cluster is possible. The MCR-ALS and DCLS images were extremely similar. The magnesium stearate sig-

nal was only observed in PC7; the low concentration of magnesium stearate, coupled with a relatively weak Raman cross-section, may account for its weak contribution to the data cube.

2. Pharmaceutical applications

Conventional Raman spectroscopy is particularly well suited to the study of the solid state of an API and has been used extensively to establish the crystalline or amorphic nature of samples. The spatial dimension introduced by Raman mapping has therefore largely been utilised to assess API solid state distribution within samples (Table 1). Raman mapping has been used to investigate API distribution differences between low and good recovery systems containing less than 1% (w/w) alprazolam (API) (Šašić, 2007b). The low API content, and relatively weak signal thereof, impeded the use of NIR chemical imaging to map API distribution. For several samples a 1950 μm × 2187 μm area (25 μm × step, 27 μm *y* step) was mapped using a point scan system. Acceptable spectral data was obtainable at 5 s per point rather than the 10 s per point used. Adoption of 5 s would have reduced the total time required per map, however, the reduction in spectral acquisition time is not linear with total acquisition time. A point scan configuration requires time for stage movement which is unalterable. Prior to the collection of spectral data the tablets of this study were trimmed to ensure a flat surface. The quality of laser focus on the sample greatly influences the collected signal, for high quality surface chemical maps samples should be flat. The importance of a flat surface increases with magnification, the higher the objective magnification the lower the depth of field, thereby increasing the need for careful sample surface preparation. Appropriate selection of objective magnification is dependent on depth of field and required spatial resolution. Spatial resolution in a point scan system is generally dependent on the objective–excitation wavelength pairing (Eq. (1)); most point scan systems are design such that the stage has a spatial resolution smaller than the minimum defined by available objective–excitation wavelength pairings. The spatial resolution required is governed by expected domain sizes and aim of the experiment. Finer resolution mapping measurements require a greater total acquisition time and more careful sample presentation.

A univariate approach to the analysis of API distribution in 0.4 and 0.8% (w/w) alprazolam tablets proved uninformative in this instance and a multivariate approach was subsequently adopted. The alprazolam information rich spectral region 580–720 cm^{-1} was subjected to PCA. The loading of PC4 mirrored the spectra of alprazolam, however, the low associated variance of this PC indicated it was susceptible to spectral noise. The score image based on PC4 was complex and indicated a need for binarization. Binarization requires careful selection of thresholds to highlight the component of interest, thresholds which are often determined through an iterative approach. The binarized scores image had twice as many pixels attributable to alprazolam than the API content would imply, however, it should not be assumed that pixel percentage in one plane is equivalent to weight percentage of API. In both the 0.4 and 0.8% (w/w) alprazolam tablets API domain size did not exceed 75 μm × 75 μm and no significant differences were observed between good and low recovery batches.

Confocal Raman mapping may be used to assess distribution beyond the surface and has been utilised to understand the shape of an amorphous domain within a crystalline sample (Ward et al., 2005). Problems encountered during formulation are increasingly being attributed to the production of the API amorphous state during processing. The production of amorphous material may be particularly problematic for inhalation devices as the detrimental characteristics associated with amorphous material are often attributed to an alteration of interfacial properties. Confocal Raman microscopy has been used to investigate the three-dimensional distribution of an amorphous domain induced in a crystalline sample (sorbitol) (Ward et al., 2005). A univariate intensity independent method of analysis was used to illustrate the cone shaped amorphous region in the sorbitol crystalline sample. The intensity of the Raman signal weakens as the laser focal point is shifted further below the surface, thereby decreasing the signal to noise ratio. By using the FWHM of the C–C–O stretching band (878 cm^{-1}), which was 34 cm^{-1} in amorphous sorbitol and 15 cm^{-1} in crystalline sorbitol, the deleterious effects of decreased signal to noise were minimised. The amorphous Raman spectrum of a sample is often characterised by broader peaks than the crystalline form due to a decreased uniformity of environment. The amorphous domain was stated to reach a maximum depth of 20 μm; no discussion was given to the problems associated with accurately determining sampling depth in a confocal Raman experiment. However, despite the inaccuracy associated with axial distance measures relative distributional information may be sourced.

The ability to depth profile makes confocal Raman microscopy an attractive technique for the study of drug diffusion through membranes (Caspers et al., 2002; Gotter et al., 2008; Zhang et al., 2007). The diffusion of the anti-psoriatic drug dithranol through an artificial acceptor membrane [dodecanol collodion (DDC) membrane – a human skin substitute] has been followed using confocal Raman microscopy (Gotter et al., 2008). This study acknowledged the difficulties associated with depth resolution within a confocal Raman experiment. Metallurgical objectives were used in the experiment leading a large refractive index change from air to the sample. Mapping of a 45 μm × 210 μm area at three levels, surface, 10 μm and 20 μm below the surface as defined by stage movement, was carried out. The authors calculated the sampling extremes of these measurements (Table 2) using the equation suggested by Everall (2000a), however, this equation does not take into account the size of the aperture and so is not representative of the confocal situation. The collected spectra were baseline corrected and normalised to the DDC membrane band at 848 cm^{-1}; the 616 cm^{-1} band was integrated to assess the distribution of dithranol. The heterogeneity of dithranol within the third layer (the layer than encompasses the membrane-drug solution interface) suggested the contact between the ointment, sample holder and membrane was not equal. In the upper most mapped level detectable amounts of dithranol were centralised over the ointment reservoir. In the middle and lower levels there were increasing amounts of drug, and at larger lateral distances from the reservoir.

The confocality of Raman mapping has also been taken advantage of in the assessment of pharmaceutical distribution within cells. Raman mapping may prove invaluable in the understanding of cellular uptake of pharmaceuticals. Liposomes have been used for intracellular drug deliver though the mechanisms of interaction between cells and liposomes are not entirely understood, especially those of liposomes modified with cell-penetrating peptides, e.g., the HIV-1 trans-activating transcriptional activator-derived TAT peptide (Matthhäs et al., 2008). The uptake of unmodified and TAT peptide modified liposomes into human breast carcinoma MCF-7 cells has been investigated using Raman mapping (Matthhäs et al., 2008). The hydrogen atoms of the two disteoroyl side chains of the 1,2-disteoroyl-d_{70}-*sn*-glycero-3-phosphocholin liposomes were replaced with deuterium. This was done to provide distinct marker bands in the 2000–2310 cm^{-1} spectral region. Cells fixed to CaF_2 windows rather than glass slides were used in this study. Ordinary glass substrates may be problematic due to fluorescence inducing impurities and should be tested prior to use. The fixed cells were immersed in a buffer solution throughout measurement which required the use of a water immersion objective; this also reduced distortion of sampling depth and prevented cell drying through the time of measurement. Sample heating is

Table 1
A summary of selected Raman mapping studies.

Problem	Sample type	Constituents	Instrumental parameters[a]	**Analysis**	**Reference**
Surface distribution of API after manufacure	Silicone elastomer reservoir-type vaginal rings	Silcone elastomer TMC120 Tetrapropyl orthosilicate Tin(II) 2-ethyl-hexanoate	785 nm, 100 mW, ⌀100 μm, 1 s and 120 s, PS, Δ100 μm, 160–225 mm^2	Principal components analysis	Bell et al. (2007)
API distribution as a function of depth	Stent coating	Rapamycin Poly(lactic-co-glycolic acid)	532 nm, confocal, 100× (0.90), 0.3 ms, 500–3500 cm^{-1}, PS, Δ0.33 μm, 700 μm^2, 32 min	Augmented classical least squares	Belu et al. (2008)
API solid state and particle size distribution	Hot melt solid dispersion	Nimodipine Polyethylene glycol 4000	632 nm, confocal (50 μm), 100×, 10 s, PS, Δ0.3 μm, 225–900 μm^2	Ratio of two peaks	Docoslis et al. (2007)
Constituent distribution after granulation	Granules after tumbling or high shear granulation	Ethenzamide Lactose Corn starch Methyl-cellulose	785 nm, 100 mW, 10 s, PS, 10,000 μm^2	Normalised peak intensity	Fujimaki et al. (2009)
Penetration of API into artificial memebrane	Synthetic skin membrane	Dithranol DDC membrane	785 nm, 100 mW, confocal (50 μm), 50×, 90 s, 75–1535 cm^{-1}, PS, Δ3 μm, 9450 μm^2	Normalised peak area	Gotter et al. (2008)
API solid state and distribution	Closed melted solid dispersions	Troglitazone Polyvinylpyrrolidone	633 nm, confocal, ⌀2 μm, 50×, PS, Δ400 spectra/200 μm^2, 200 μm^2	FWHM of peak Peak intensity	Furuyama et al. (2008)
Chemically identify particles and subsequently particle size and particle size distribution	Aqueous nasal spray suspension	Beclomethasome dipropionate Microcrystalline cellulose Carboxymethyl cellulose Benzalkoniium chloride Polysorbate 80 Phenylethyl alcohol	532 nm, 160 mW, ⌀50 μm, 50×, 40 s, global, Δ0.3 μm/pixel, 39,800–826,875 μm^2, 200 min		Doub et al. (2007)
API solid state and distribution	Tablets	Chloramphenicol palmitate	633 nm, 5 mW, confocal (1100 μm), ⌀3 μm, 50×, 3 s, 702–1625 cm^{-1}, PS, Δ3 μm, 8100 μm^2	Multivariate image segmentation using a spatial directed agglomeration clustering method	Lin et al. (2006)
Differentiation of amorphous drug molecular dispersions and nanodispersions	Solid dispersion	Felodipine Polyvinylpyrrolidone	632 nm, 30 mW, confocal (50 μm), 100×, 10 s, PS, Δ0.1 μm, 36 μm^2	Peak intensity ratios	Karavas et al. (2007)
Uptake and distribution of peptide modifed liposomes into cells	Liposomes	MCF-7 cells Deuterated 1,2-distearoyl-d_{70}-*sn*-glycero-3-phosphocoline Deuterated TATp modified 1,2-distearoyl-d_{70}-*sn*-glycero-3-phosphocoline	488 nm, 30 mW, confocal, 60× water immersion (1.00), 0.5 s, 200–4500 cm^{-1}, PS, Δ0.5 μm, 2400 μm^2	Peak intensity	Matthhäs et al. (2008)
API solid state	Thermal inkjet dispensed API	Prednisolone	785 nm, ⌀1–2 μm, 10 s, 150–750 cm^{-1}, PS, Δ5 μm in x direction 1 μm in y direction, 10,500–12,000 μm^2	Signal-to-baseline (peak area)	Meléndez et al. (2008)
API distribution	Transdermal tape	Tulobuterol Rubber matrix Acrylic matrix Tape	785 nm, 100 mW, 10 s, PS, Δ2 μm, 10,000–40,000 μm^2	Peak area	Sakamoto et al. (2009)
Characterise aerosol particulate deposits	Pressurized metered-dose inhaler deposits	Ventide (Allen and Hanbury, UK) contains: Salbutamol Beclomethasome dipropionate	785 nm, 10 mW, 50×, 30 s, 1338–1829 cm^{-1}, PS, Δ1 μm, 10,000 μm^2	Ratio of peak area	Steele et al. (2004)
API distribution	Low API content tablets	Oleic acid 0.4% (w/w) API tablets 0.8% (w/w) API tablets API – alprazolam	782 nm, ⌀26 μm, 20×, 10 s, 550–1120 cm^{-1}, PS, Δ25 μm in *x* direction 27 μm in *y* direction, 4.3 mm^2, 24 h	Univariate Principal components analysis Binarization	Šašić (2007a)
Constituent distribution after different manuacturing processes	Tablets	Undisclosed API Microcrystalline cellulose Dicalcium phosphate Sodium starch Glycolate Magnesium stearate	782 nm, 100 mW, 20×, PS, Δ25 μm, 4 mm^2, 21 h	Peak intensity – selection of peak guided by orthogonal projection approach Principal components analysis Binarization	Šašić (2007b)

Table 1 (*Continued*)

Problem	Sample type	Constituents	Instrumental parameters[a]	**Analysis**	**Reference**
Assess performance of line-mapping and global imaging platforms for identifying constituent distribution	Tablets Powder blend	Undisclosed API Microcrystalline cellulose Dicalcium phosphate Sodium starch Glycolate Magnesium stearate	782 nm, ⌀10 μm, 20× (0.46), 60 s, 900–1432 cm^{-1}, line mapping, 56 μm line, 90,000 μm^2, 2.5 h 782 nm, ⌀10 μm, 50× (0.50), 30 s, 900–1432 cm^{-1}, line mapping, 20 μm line, 90,000 μm^2, 3.5 h 532 & 785 nm, 200–600 mW, ⌀1.3 μm, 20×, 20–60 s per wavenumber, 850–1450 cm^{-1}, global, FOV 7225 μm^2, 65,025 μm^2, 4 h 532 & 785 nm, 200–600 mW, ⌀1.3 μm, 50×, 20–60 s per wavenumber, 850–1450 cm^{-1}, global, FOV 289 μm^2, 14,400 μm^2, 24 h	Principal component analysis Peak intensity – peaks selected by orthogonal projection approach	Šašić and Clark (2006)
Constituent distribution, and API solid state and content	Tablets produced by different manufacturing processes	Imipramine HCl Microcrystalline cellulose Maize starch Hydroxypropyl-Methyl-cellulose Magnesium stearate	785 nm, confocal, ⌀4 μm, 10×, 60 s, 1630–4000 cm^{-1}, PS, Δ10 μm, 78,400–115,600 μm^2 785 nm, confocal, ⌀1 μm, 100×, 60 s, 1630–4000 cm^{-1}, PS, Δ2 μm, 14,400 μm^2	Direct classical least squares	Vajna et al. (2010)
Amorphous domain distribution	Pure sorbitol with surface amorphous domain	Sorbitol	532 nm, 100× (0.90), PS	Peak full width at half maximum height	Ward et al. (2005)
Constituent distribution	Solid lipid extrudate	Theophylline anhydrate Tripalmitin Polyethylene glycol 1000	785 nm, 100 mW, confocal (50 μm), ⌀2 μm, 100× (0.90), 15 s, 50–1530 cm^{-1}, PS, Δ2 μm, 36,000 μm^2	Peak area	Windbergs et al. (2010)
API distribution	Transdermal drug delivery device	Oestradiol Patch matrix	1064 nm, 450 mW, ⌀25–30 μm, 40×, 2000 scans, 50–3500 cm^{-1}, PS, Δ50 μm, 22,500 μm2	Visual comparison of spectra	Armstrong et al. (1996)
API and prodrug distribution as a function of depth	Pig skin	5-Flurouracil 1-ethyloxycarbonyl-5-fluorouracil Isopropyl myrisate Pig skin biopsy	785 nm, 12 mW, confocal, 100× oil immersion, 240 s, 100–3450 cm^{-1}, PS, Δ5 μm, 3600 μm^2	Normalised peak area Factor analysis	Zhang et al. (2007)
Constituent distribution	Tablets	API Inorganic binder Lubricant Diluent Disintegrant	633 or 782 nm, ⌀5 μm, 20× (0.46), 30 s, 637–1536 or 744–1630 cm^{-1}, PS, Δ20 μm, 1.4–1.9 mm^2	Peak area	Clarke et al. (2001)
Constituent distribution	Bilayer tablets	Lactose Microcrystalline cellulose Magnesium stearate Red dye (FD&C red #40) Sodium benzoate	785 nm, 50× (0.55), 71–1266 cm^{-1}, PS, Δ10 μm, 160,000 μm^2	Principal components analysis Direct classical least squares K-means clustering Fuzzy C-means clustering Multivariate curve resolution	Zhang et al. (2005)
Constitutent distribution	Tablets	Acetaminophen Lactose Microcrystalline cellulose Magnesium stearate	785 nm, 50×, 30 s, 300–1800 cm^{-1}, PS, 40,000 μm^2, ~800 min	Band-target entropy minimization SIMPLISMA	Widjaja and Seah (2008)
Permeation of penetration enhancer	Human palm	Stratum corneum Dimethyl sulfoxide	850 nm, 100 mW, confocal (100 μm) ⌀2 μm, 63×, 30 s, 400–1850 cm^{-1}, PS, Δ10 μm, 1200 μm^2	Ratio of peak areas	Caspers et al. (2002)

[a] Instrumental parameters: excitation wavelength/nm, laser power/mW, confocal (aperture size/μm), laser sampling diameter (⌀)/μm, objective (numerical aperture), spectral collection time/s, spectral region collected/cm^{-1}, instrument type (PS is a point scan system), step size (Δ)/μm, area covered by sampling plane/μm^2 or mm^2, total time of data collection/min or h.

Table 2
The apparent depth and sampling extremes of depth measurements (Gotter et al., 2008).

Layer	Stage defined depth (μm)	Minimum sampling depth (μm)	Maximum sampling depth (μm)
Bottom	1	1.47	2.46
Middle	10	14.65	24.6
Top	20	29.3	49.2

a concern when collecting Raman spectroscopic measurements, particularly when using a Raman microscope. The high power density of the tightly focussed interrogating laser may burn samples if the laser power is not carefully moderated. In addition to using a water immersion lens to dissipate heat and prevent cell drying a laser power of just 30 mW was used. Further, the sample was moved through the laser focus at a constant speed (spectra were collected from a 0.5 μm grid across a cell with a 0.5 s dwell time), this continuous motion system prevented sample degradation both through reducing sample heating and overall time of mapping measurement (~1 h per cell). Interestingly an excitation wavelength of 488 nm was used; generally near-infrared wavelengths are applied to cellular systems to reduce fluorescence. The ν^4 law of scattering dictates that the use of shorter excitation wavelengths produces stronger Raman scattering. Hence the shortest wavelength that does not induce insurmountable fluorescence and photodamage should be used to reduce spectral collection time. Despite the relatively high energy excitation wavelength (488 nm) for a cellular system fluorescence was not an issue. The CH (2800–3020 cm^{-1}) and CD (2000–2300 cm^{-1}) stretching bands were integrated to track the cellular uptake of the liposomes. The unmodified liposomes were only reproducibly observed within the cells after 12 h of incubation; at 18 and 24 h the liposome inclusions within the cells had grown to a few μm. TAT peptide modified liposome penetration of the cells was faster. After just 3 h TAT peptide modified liposomes were observed around the cell membrane and after 6 h the TAT peptide modified liposomes had penetrated well in to the cell. A further 3 h of incubation did not increase the amount of deuterated TAT peptide modified liposomes within the cells. To ensure the observed liposomes were within the cell and not just adsorbed to the surface a depth profile was recorded. The cells were approximately 10 μm thick and the axial resolution of the system claimed to be 1 μm. Deuterated liposomes were observed to be present within the cell, not adsorbed to the surface.

Medical devices are increasingly used as vehicles for drug administration, for example stents covered in coatings containing anti-proliferatives for the purpose of preventing artery re-blockage. In controlled release systems polymers are used to control drug release rate and hence there is a need to understand the drug/polymer mixture. Confocal Raman depth profiling was used to investigate the distribution of the anti-proliferative rapamycin (API) within a poly(lactic-co-glycolic acid)/rapamycin coating (Belu et al., 2008). Four levels of rapamycin concentration were examined, one of which was examined with and without the presence of a top layer of poly(lactic-co-glycolic acid) (PLGA). No crystalline rapamycin was located within the coatings and so an ACLS procedure using amorphous rapamycin and PLGA as basis spectra was applied to determine API distribution. The coatings became more heterogeneous with increased rapamycin loading and the top coat of PLGA was a distinct layer of roughly equal thickness to the rapamycin/PLGA layer. In this experiment reflection at the coating/metal interface caused an increase in the spectral background; imaging artefacts may arise from reflective surfaces or surface roughness. The use of a dry objective was justified by the odd geometry of the stents and therefore a compression of the vertical axis was expected. Despite the inability to accurately measure distance beneath the surface the information regarding distribution of rapamycin was valuable. Upon soaking the coated stents the segregation of rapamycin within the PLGA matrix increased. Within the top coated sample containing 25% (w/w) rapamycin the API was initially located in the base coat, after 26 days of soaking rapamycin had migrated throughout the PLGA top coat and after 48 days the rapamycin had fully eluted. Concentration profiles calculated on the basis of the 1640 cm^{-1} (rapamycin) and 2950 cm^{-1} (PLGA) peaks indicated the 5% (w/w) rapamycin coating would exhibit an initial burst of release followed by a fairly constant elution of API. The 50% (w/w) rapamycin coating would exhibit an even greater initial burst due to the high initial surface concentration of rapamycin, followed by less controlled drug elution due to the formation of large domains upon soaking.

The purpose of controlled release systems is to increase the efficacy of drugs and reduce dosage frequency. Solid lipid extrudates are a potential slow release matrix. To form a solid lipid extrudate a drug and lipid are extruded together below the melting point of the lipid, resulting in a lipid matrix containing dispersed API particles. The distribution of API within the lipid matrix is paramount to determining the release properties of these systems. Raman mapping has been used to map regions of the outer surface and cross-section of solid lipid extrudates containing tripalmitin, theophylline anhydrate with and without polyehtlene glycol 10,000 (Windbergs et al., 2010). Component specific peaks were integrated and normalised to the most intense peak for that specific component. The threshold level for display of integrated peak areas was investigated and a compromise between overlapping regions and empty area reached to give a threshold of 8%. The extrudate devoid of polyethylene glycol had a continuous lipid phase with a wide range of theophylline particle sizes. Lipid and theophylline were more intimately mixed at the surface of the extrudate than in the cross-section. When polyethylene glycol was included in the extrudate all three constituents were present at the surface. No preferential associations were encountered between the three components. Extending on this distributional study the extrudates were chemically mapped after a specific time of dissolution. A uniform receding boundary was not encountered in distributional assessment of post-dissolution extrudates. Sample preparation of extrudates post-dissolution for Raman mapping measurements was complicated by a loss of structural integrity which made the cutting of a flat surface perpendicular to the axis of the extrudate difficult.

The API distribution of a silicone elastomer based controlled drug release system has also been investigated by Raman mapping (Bell et al., 2007). In this case however, a 'macro' rather than microscopic system was used. The domains of interest in a distributional study of TMC120 within a reservoir-type vaginal ring exceeded 100 μm thereby allowing the use of an interrogating laser diameter of 100 μm. In manufacture the core is loaded with an excess of TMC120 and then surrounded by a non-medicated sheath. The solubility of TMC120 within the silicone elastomer of the vaginal ring was low so that any spectrum displaying drug bands indicated the presence of TMC120 concentration well above the saturation value and therefore a reservoir of undissolved drug in the ring. Principal components analysis was used to produce chemical maps illustrating the distribution of TMC120. A sharp decrease in drug content across the core/sheath interface was expected, however, a gradual decrease was observed; drug migration was occurring during manufacture or storage. A time series measurement of the vaginal ring from two to 30 h after manufacture indicated there was no movement of TMC120. Examining TMC120 distribution of vaginal rings produced using two temperatures (25 and 80 °C) indicated there was no significant difference in the concentration at the core/sheath boundary. Despite the inability to explain the mechanism of drug migration across the core/sheath boundary the utility of Raman mapping in drug distribution characterisation was clearly shown.

Active pharmaceutical ingredients are combined with polymers not only for the purposes of controlled release. Several approaches for enhancing API solubility have been identified, for example using the amorphous form of the API or formulation within a polymer based solid dispersion. For example, formulation within a polyvinlypyrrolidone solid dispersion to increase troglitazone solubility has been suggested (Furuyama et al., 2008). Troglitazone has two asymmetric carbons, the result of which is that it is produced as a mixture of four isomers. Raman mapping was used to determine the effect of solid dispersion processing conditions (different temperatures and water contents) on the solid state of troglitazone. The FWHM of the troglitazone specific 1747 cm^{-1} band was used to determine crystalline and amorphous regions within the solid dispersions. Increased preparation temperature and water content increased the size of amorphous domains. Peaks characteristic to the two crystalline isomer pairs were used to determine the distribution of the L-pair and H-pair crystalline forms. By assessing the distribution of the various troglitazone forms it was postulated that the L-pair dissolved in the rubbery PVP to a greater extent than the H-pair. The highly overlapping distributions of PVP and amorphous troglitazone suggested the amorphous form was produced after the dissolution of crystalline troglitazone within rubbery PVP. Nimodipine is another drug for which solid dispersions have been used to increase solubility (Docoslis et al., 2007). As with troglitazone the solid state nature of nimodipine is complicated by enantiomers. Two modifications of nimodipine were investigated: modification I – the crystalline form containing both the *d* and *l* forms within a unit cell, and modification II – an equimolar mixture of the crystalline *d* and the crystalline *l* forms, also known as the conglomerate. Within the Raman spectra the band intensity ratio of the C=C stretch of the dihydropyridine ring (1642 cm^{-1}) to the $-NO_2$ group stretch (1347 cm^{-1}) was a point of difference between the three solid states: average $I_{1347/1652} = 3.67$ for modification I, average $I_{1347/1652} = 1.22$ for the amorphous form and average $I_{1347/1652} = 0.171$ for modification II. As these two bands did not overlap with those of the dispersion matrix, polyethylene glycol, Raman chemical maps were constructed on the basis of this band ratio. In the resulting analysis however large areas were not readily classifiable as completely crystalline or amorphous ($0.25 < I_{1347/1652} < 3.5$). Examination of the raw spectral data from regions where $I_{1347/1652}$ was greater than 3.5 indicated these areas were definitely modification I areas, and those where $I_{1347/1652}$ was less than 0.25 were definitely modification II areas, however between these extremes a heterogenous state existed. It was speculated that these areas contained crystals of nimodipine of sub-μm dimensions and/or amorphous regions. The authors did observe that there were wavenumbers shifts in the bands of nimodipine, occasionally up to 4 cm^{-1} difference, and these shifts may have lead to erroneous calculation of the band intensities. It is important if using a system without internal wavenumber axis calibration that the stability of the wavenumber axis over the time and conditions of a mapping measurement is assessed. Band shift changes associated with instrumental variation will be detrimental to any analysis, particularly tightly constrained univariate analyses.

Nasal drug delivery is an alternative to oral dosage forms. Raman mapping has been used to identify and size particles within a nasal spray formulation (Doub et al., 2007). Validation of Raman image based particle size measurements with NIST-traceable polystyrene standards indicated Raman images lead to overestimation of particle size. It was suggested this was probably a result of an inability to accurately define the particle edges. Measurement of several particles at once, and subsequent averaging, lead to results which were not significantly different to those of the polystyrene bead supplier. The overestimation of particle diameter was systematic and appropriate binary thresholding criteria, e.g., signal to noise ratio of spectra, would minimise this. The particle size distribution of the nasal spray formulation was different pre- and post-formulation, an observation that could not be attributed to the excipient particles as the API Raman signature was very distinct. High variability was associated with replicate measurements however, perhaps indicating need for sampling a greater number of API particles.

The uniformity of constituent distribution for different granulation processes has been assessed using Raman chemical mapping (Fujimaki et al., 2009). In a system containing ethenzamide, lactose, corn starch and methyl cellulose the high dispersibility of methyl cellulose was evident as this component had a highly uniform distribution early in the granulation process and had domain sizes independent of particle size. The respective domains sizes of the other three components were influenced by particle size. Constituent distribution was found to be dependent on aggregation characteristics of each ingredient, type of granulation method or granulation time. With increasing time of granulation corn starch and lactose had a tendency to overlap, this suggested that in addition to the previously mentioned characteristics interactions of ingredients affected distributional properties.

It is possible to use Raman mapping to examine the effects of different manufacturing methods. Seven methods of manufacture of an imipramine hydrochloride based tablet system were investigated using both high and low spatial resolution (Vajna et al., 2010). Using DCLS constituent density maps were plotted and interpreted in terms of the manufacturing process. The different manufacturing methodologies lead to repeatedly distinct Raman chemical images. For high concentration constituents low resolution images imparted the same informational trends as high resolution images. Examination of minor components, for example the lubricant magnesium stearate, required the fine detail offered by the high resolution mapping measurements. Altering compaction force did not alter constituent distribution but did alter intensity of the overall Raman signal. With greater compaction the density of the sample increased and therefore more molecules were present within the sampling volume leading to greater Raman intensities. It was shown that the DCLS scores calculated for the maps could be used in consideration with the dosage of the tablet to generate an approximation of constituent concentration.

Raman spectroscopy is not appropriate for all pharmaceutical situations and often best employed in conjunction with other analytical techniques, especially mid- or near-infrared spectroscopies. Raman and infrared spectroscopies are complementary; fusion of mapping data acquired through the use of these techniques more completely describes the system under investigation. Fusion of imaging techniques requires the measurement of spectra from the same section of a sample. This data is subsequently analysed to determine individual constituent distributions. A fused image is created by first deciding which form of spectroscopy used offers the most robust constituent distribution. The chosen distributions for each of the constituents are then combined to form a composite image. This process is known as chemical image fusion (Clarke et al., 2001). The fusion of NIR and Raman mapping data has been used to investigate tablet processing problems (Clarke et al., 2001). During tabletting a formulation containing API, inorganic binder, lubricant, diluent and a disintegrant was found to occasionally stick to the tablet tooling. Initially it was assumed that this was a function of poor lubricant distribution within the tablets and subsequently good and sticking blends were imaged. Because of the chemical nature of the constituents Raman spectroscopy was not appropriate for the mapping of disintegrant distribution and near-infrared spectroscopy was not appropriate for the mapping of the inorganic binder. In the fused image the API and inorganic binder distributions were taken from the Raman mapping data and the remaining constituent distributions from the NIR data. The resulting fused images of the good and sticking blends indicated the lubricant distribution was equivalent in both. The distribution of

inorganic binder and diluent was different between the blends; in the good blend the inorganic binder was present in larger particle sizes (40–150 μm vs. 20–50 μm) and less intimately mixed with the diluent. It is foreseeable that as vibrational spectroscopic mapping instrumentation becomes more widely available the advantages of chemical image fusion will be more widely utilised.

3. Conclusions

Raman mapping may be used for component distribution assessment in a wide range of areas, e.g., controlled release devices, penetration of membranes, cellular uptake of delivery systems, characterisation of different tabletting methodologies and investigation of processing problems. Many of these studies have utilised the confocal arrangement offered by Raman microscopy successfully despite the difficulties associated with accurately determining sampling depth. At present, Raman mapping has largely been hampered by the time required to collect a representative data set, and the advent of faster spectral collection systems is likely to increase interest in the application of Raman mapping to a greater variety of pharmaceutical systems. Further, the greater availability of vibrational spectroscopic imaging systems will lead to a greater utilisation of the synergy offered by Raman and infrared spectroscopies.

References

Amigo, J.M., Cruz, J., Bautista, M., Maspoch, S., Coello, J., Blanco, M., 2008. Study of pharmaceutical samples by NIR chemical-image and multivariate analysis. TrAC, Trends Anal. Chem. 27, 696–713.

Amigo, J.M., Ravn, C., 2009. Direct quantification and distribution assessment of major and minor components in pharmaceutical tablets by NIR-chemical imaging. Eur. J. Pharm. Sci. 37, 76–82.

Andrew, J.J., Hancewicz, T.M., 1998. Rapid analysis of Raman image data using two-way multivariate curve resolution. Appl. Spectrosc. 52, 797–807.

Armstrong, C.L., Edwards, H.G.M., Farwell, D.W., Williams, A.C., 1996. Fourier transform Raman microscopic study of drug distribution in a transdermal drug delivery device. Vib. Spectrosc. 11, 105–113.

Bell, S.E.J., Dennis, A.C., Fido, L.A., Malcom, R.K., Sirimuthu, N.M.S., Toner, C.F., Woolfson, A.D., 2007. Characterization of silicone eleastomer vaginal rings containing HIV microbicide TMC120 by Raman spectroscopy. J. Pharm. Pharmacol. 59, 203–207.

Belu, A., Mahoney, C., Wormuth, K., 2008. Chemical imaging of drug eluting coatings: combining surface analysis and confocal Raman microscopy. J. Control. Release 126, 111–121.

Caspers, P.J., Williams, A.C., Carter, E.A., Edwards, H.G.M., Barry, W.B., Bruining, H.A., Puppels, G.J., 2002. Monitoring the penetration enhancer dimethyl sulfoxide in human stratum corneum *in vivo* by confocal Raman spectroscopy. Pharm. Res. 19, 1577–1580.

Clarke, F.C., Jamieson, M.J., Clark, D.A., Hammond, S.V., Jee, R.D., Moffat, A.C., 2001. Chemical image fusion. The synergy of FT-NIR and Raman mapping microscopy to enable a more complete visualization of pharmaceutical formulations. Anal. Chem. 73, 2213–2220.

Cruz, J., Bautista, M., Amigo, J.M., Blanco, M., 2009. NIR-chemical imaging study of acetylsalicylic acid in commercial tablets. Talanta 80, 473–478.

Deckert, V., Zeisel, D., Zenobi, R., Vo-Dinh, T., 1998. Near-field surface enhanced Raman imaging of dye-labelled DNA with 100 nm resolution. Anal. Chem. 70, 2646–2650.

Docoslis, A., Huszarik, K.L., Papageorgiou, G.Z., Bikiaris, D., Stergiou, A., Georgarakis, E., 2007. Characterisation of the distribution, polymorphism, and stability of nimodipine in its solid dispersions in polyethylene glycol by micro-Raman spectroscopy and powder x-ray diffraction. AAPS J. 9, Article 43.

Doub, W.H., Adams, W.P., Spencer, J.A., Buhse, L.F., Nelson, M.P., Treado, P.J., 2007. Raman chemical imaging for ingredient-specific particle size characterization of aqueous suspension nasal spray formulations: a progress report. Pharm. Res. 24, 934–945.

Duponchel, L., Elmi-Rayaleh, W., Ruckebusch, C., Huvenne, J.P., 2003. Multivariate curve resolution methods in imaging spectroscopy: influence of extraction methods and instrumental perturbations. J. Chem. Inf. Comput. Sci. 43, 2057–2067.

Everall, N.J., 2000a. Modeling and measuring the effect of refraction on the depth resolution of confocal Raman microscopy. Appl. Spectrosc. 54, 773–782.

Everall, N.J., 2000b. Confocal Raman microscopy: why the depth resolution and spatial accuracy can be much worse than you think. Appl. Spectrosc. 54, 7515–7520.

Everall, N., Lapham, J., Adar, F., Whitley, A., Lee, E., Mamedov, S., 2007. Optimizing depth resolution in confocal Raman microscopy: a comparison of metallurgical, dry corrected, and oil immersion objectives. Appl. Spectrosc. 61, 251–259.

Fujimaki, Y., Matsubara, T., Sakamoto, T., Sasakura, D., Miura, T., Takekawa, M., Hiyama, Y., 2009. Distribution of ethenzamide and other ingredients on granule surfaces studied by Raman microspectroscopy and mapping. Pharmazie 64, 316–322.

Furuyama, N., Hasegawa, S., Hamaura, T., Yada, S., Nakagami, H., Yonemochi, E., Terada, K., 2008. Evaluation of solid dispersion on a molecular level by the Raman mapping technique. Int. J. Pharm. 361, 12–18.

Geladi, P., Grahn, H. (Eds.), 1997. Multivariate Image Analysis. John Wiley & Sons Inc, New York.

Gendrin, C., Roggo, Y., Collet, C., 2007. Content uniformity of pharmaceutical solid dosage forms by near infrared hyperspectral imaging: a feasibility study. Talanta 73, 733–741.

Gendrin, C., Roggo, Y., Collet, C., 2008. Pharmaceutical applications of vibrational chemical imaging and chemometrics: a review. J. Pharm. Biomed. Anal. 8, 533–553.

Gotter, B., Faubel, W., Neubert, R.H.H., 2008. FTIR microscopy and confocal Raman microscopy for studying lateral drug diffusion from a semisolid formulation. Eur. J. Pharm. Biopharm. 74, 14–20.

Grahn, H.F., Geladi, P. (Eds.), 2007. Techniques and Applications of Hyperspectral Image Analysis. John Wiley & Sons Ltd, Chichester.

Hamad, M.L., Ellison, C.D., Khan, M.A., Lyon, R.C., 2007. Drug product characterization by macropixel analysis of chemical images. J. Pharm. Sci. 96, 3390–3401.

Juang, C.B., 1998. Design and application of a computer-controlled confocal scanning differential polarization microscope. Rev. Sci. Instrum. 59, 2399–2408.

Karavas, E., Georgarakis, M., Docoslis, A., Bikiaris, D., 2007. Combining SEM, TEM, and micro-Raman techniques to differentiate between the amorphous molecular level dispersions and nanodispersions of a poorly water-soluble drug within a polymer matrix. Int. J. Pharm. 340, 76–83.

Kolomiets, O., Hoffmann, U., Geladi, P., Siesler, H.W., 2008. Quantitative determination of pharmaceutical drug formulations by near-infrared spectroscopic imaging. Appl. Spectrosc. 62, 1200–1208.

Lin, W.-Q., Jiang, J.-H., Yang, H.-F., Ozaki, Y., Shen, G.-L., Yu, R.-Q., 2006. Characterizatioin of chloramphenicol palmitate drug polymorphs by Raman mapping with multivariate image segmentation using a spatial directed agglomeration clustering method. Anal. Chem. 78, 6003–6011.

Long, D.A., 2002. The Raman Effect: A Unified Treatment of the Theory of Raman Scattering by Molecules. John Wiley & Sons Ltd., London.

Long, D.A., 2005. Introduction to Raman spectroscopy. In: Edwards, H.G.M., Chalmers, J.M. (Eds.), Raman Spectroscopy in Archaeology and Art History. Royal Society of Chemistry, Cambridge.

Matthhäs, C., Kale, A., Chernenko, T., Torchilin, V., Diem, M., 2008. New ways of imaging uptake and intracellular fate of liposomal drug carrier systems inside individual cells, based on Raman microscopy. Mol. Pharm. 5, 287–293.

McCreery, R.L., 2000. Raman Spectroscopy for Chemical Analysis. John Wiley & Sons Inc., New York.

Meléndez, P.A., Kane, K.M., Ashvar, C.S., Albrecht, M., Smith, P.A., 2008. Thermal inkjet application in the preparation of oral dosage forms: dispensing of prednisolone solutions and polymorphic characterization by solid-state spectroscopic techniques. J. Pharm. Sci. 97, 2619–2636.

Pappas, D., Smith, B.W., Winefordner, J.D., 2000. Raman imaging for two-dimensional chemical analysis. Appl. Spectrosc. Rev. 35, 1–23.

Raman, C.V., 1928. A change of wave-length in light scattering. Nature 128, 619.

Raman, C.V., Krishnan, K.S., 1928. A new type of secondary radiation. Nature 121, 501–502.

Raman, C.V., Krishnan, K.S., 1929. The production of new radiation by light scattering. Part I. Proc. R. Soc. Lond. 122, 23–34.

Sakamoto, T., Matsubara, T., Sasakura, D., Takada, Y., Fujimaki, Y., Aida, K., Miura, T., Terahara, T., Higo, N., Kawanishi, T., Hiyama, Y., 2009. Chemical mapping of tulobuterol in transdermal tapes using microscopic laser Raman spectroscopy. Pharmazie 64, 166–171.

Šašić, S., Clark, D.A., Mitchell, J.C., Snowden, M.J., 2004. A comparison of Raman chemical images produced by univariate and multivariate data processing—a simulation with an example from pharmaceutical practice. Analyst 129, 1001–1007.

Šašić, S., Clark, D.A., 2006. Defining a strategy for chemical imaging of industrial pharmaceutical samples on Raman line-mapping and global illumination instruments. Appl. Spectrosc. 60, 494–502.

Šašić, S., 2007a. An in-depth analysis of Raman and near-infrared chemical images of common pharmaceutical tablets. Appl. Spectrosc. 61, 239–250.

Šašić, S., 2007b. Raman mapping of low-content API pharmaceutical formulations I. Mapping of alprazolam in Alprazolam/Xanax tablets. Pharm. Res. 24, 58–65.

Smith, E., Dent, G., 2005. Modern Raman Spectroscopy—A Practical Approach. John Wiley & Sons Ltd, Chichester.

Steele, D.F., Young, P.M., Price, R., Smith, T., Edge, S., Lewis, D., 2004. The potential use of Raman mapping to investigate *in vitro* deposition of combination pressurized metered-dose inhalers. AAPS J. 6, Article 32.

Tabaksblat, R., Meier, R.J., Kip, B.J., 1992. Confocal Raman microspectroscopy: theory and application to thin polymer samples. Appl. Spectrosc. 46, 60–68.

Vajna, B., Farkas, I., Szabó, A., Zsigmond, Z., Marosi, G., 2010. Raman microscopic evaluation of technology dependent structural differences in tablets containing imipramine model drug. J. Pharm. Biomed. Anal. 51, 30–38.

Ward, S., Perkins, M., Zhang, J., Roberts, C.J., Madden, C.E., Luk, S.Y., Patel, N., Ebbens, S.J., 2005. Identifying and mapping surface amorphous domains. Pharm. Res. 22, 1195–1202.

Widjaja, E., Seah, R.K.H., 2008. Application of Raman spectroscopy and band-target entropy minimization to identify minor components in model pharmaceutical tablets. J. Pharm. Biomed. Anal. 46, 274–281.

Windbergs, M., Haaser, M., McGoverin, C.M., Gordon, K.C., Kleinebudde, P., Strachan, C.J., 2010. Investigating the relationship between drug distribution in solid lipid matrices and dissolution behaviour using Raman spectroscopy and mapping. J. Pharm. Sci. 99, 1464–1475.

Zhang, L., Henson, M.J., Sekulic, S.S., 2005. Multivariate data analysis for Raman imaging of a model pharmaceutical tablet. Anal. Chim. Acta 545, 262–278.

Zhang, G., Moore, D.J., Sloan, K.B., Flach, C.R., Mendelsohn, R., 2007. Imaging the prodrug-to-drug transformation of a 5-fluorouracil derivative in skin by confocal Raman microscopy. J. Invest. Dermatol. 127, 1205–1209.